

# MDHP-Net: Detecting Injection Attacks on In-vehicle Network using Multi-Dimensional Hawkes Process and Temporal Model

Qi Liu<sup>†</sup>, Yanchen Liu<sup>†</sup>, Ruifeng Li, Chenhong Cao, Yufeng Li\*, Xingyu Li\*, Peng Wang, Runhan Feng

**Abstract**—The integration of intelligent and connected technologies in modern vehicles, while offering enhanced functionalities through Electronic Control Unit and interfaces like OBD-II and telematics, also exposes the vehicle’s in-vehicle network (IVN) to potential cyberattacks. In this paper, we consider a specific type of cyberattack known as the injection attack. As demonstrated by empirical data from real-world cybersecurity adversarial competitions<sup>1</sup>, these injection attacks have excitation effect over time, gradually manipulating network traffic and disrupting the vehicle’s normal functioning, ultimately compromising both its stability and safety. To profile the abnormal behavior of attackers, we propose a novel injection attack detector to extract long-term features of attack behavior. Specifically, we first provide a theoretical analysis of modeling the time-excitation effects of the attack using Multi-Dimensional Hawkes Process (MDHP). A gradient descent solver specifically tailored for MDHP, MDHP-GDS, is developed to accurately estimate optimal MDHP parameters. We then propose an injection attack detector, MDHP-Net, which integrates optimal MDHP parameters with MDHP-LSTM blocks to enhance temporal feature extraction. By introducing MDHP parameters, MDHP-Net captures complex temporal features that standard Long Short-Term Memory (LSTM) cannot, enriching temporal dependencies within our customized structure. Extensive evaluations demonstrate the effectiveness of our proposed detection approach.

## 1. Introduction

Connected and automated vehicles (CAVs) integrate numerous Electronic Control Units (ECUs), which are interconnected through various types of In-Vehicle Networks (IVNs), such as Controller Area Networks (CAN), Local Interconnect Networks (LIN), and FlexRay, to control various vehicle functionalities. Furthermore, interfaces including the OBD-II port, sensors, and telematics facilitate communication between the IVN and the external environment. These interfaces provide notable benefits, such as mitigating traffic congestion, enhancing driving convenience, and promoting driving safety [1].

Attacks on the IVN or ECUs pose significant threats to the safety and stability of CAVs. Many research has focused

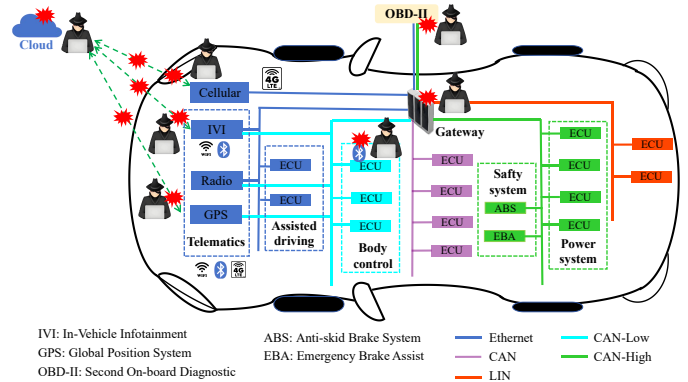


Figure 1: The vulnerabilities of IVN. It covers ECU and their connections, including communication protocols like Ethernet, CAN (high and low speed), and LIN. Key components such as the IVI system, GPS, and ABS are highlighted, showing their connections through the gateway and potential external threats from sources like the cloud and OBD-II interface [2].

on identifying and analyzing the vulnerabilities of CAVs [3][4][5]. Figure 1 shows the typical attacker’s view of CAV IVN’s vulnerability. As CAVs are increasingly equipped with various interfaces (e.g., OBD-II, TCU, Gateway) to interact with external entities (e.g., diagnostic tools, remote servers, and telematics systems), attackers are finding new ways to exploit these interfaces and attack the vehicles. For instance, vulnerabilities in the OBD-II interface allow adversaries to inject malicious commands into the low-speed and high-speed CAN buses, affecting critical systems such as body control, powertrain, and safety systems [6][7]. Additionally, researchers have shown that vulnerabilities in aftermarket vehicle diagnostic tools can be exploited to remotely control various vehicle functions, such as doors, windows, and mirrors [8]. Notable examples include security researchers demonstrating vulnerabilities in Jeep [9], BMW [10] and Tesla’s Model S and X [11], successfully hacking into vehicle systems to remotely control various functions, including doors, brakes, and keyless entry. Each of these attacks was executed by injecting specific data into the vehicle’s IVN through exposed interfaces.

In this paper, we concentrate a time-excitation injection attack in IVN identified through observations of real-world cyberattack and defense data. Table 1 presents a statistical

1. “Qiangwang” International Elite Challenge On Cyber Mimic Defense: [mimic2024.xctf.org.cn](http://mimic2024.xctf.org.cn). Due to data sensitivity, access requires prior authorization.

summary of attacks on autonomous driving control systems recorded during the “Qiangwang” International Elite Challenge On Cyber Mimic Defense<sup>1</sup>. Initially, attacks on the target control system appeared negligible. However, the frequency of attacks escalated over time, exhibiting a sharp upward trend. Insights from experienced hackers suggest that attackers, by persistently probing with various tools, such as injection attacks, are more likely to identify vulnerabilities and exploit the system’s weakness. In this scenario, the likelihood of a successful attack is influenced by previous attempts, as past failures accumulate, thereby increasing the probability of success in subsequent attempts.

Table 1: Cybersecurity Test Data for Autonomous Driving Control System. The Challenge lasts a total of 72 hours, encompassing both the number of times hackers attempt to attack the target system and the final number of successful vulnerabilities exploited.

Test Type / Time (Hours)	5	12	35	56	70	72
Number of Attacks	26	1010	20910	161559	535002	537252
Number of Vulnerabilities	0	1	60	239	316	330

To identify injection attacks in IVN, existing countermeasures can be divided into two categories [12]: the security enhancement of IVN protocols and intrusion detection. The security enhancement of IVN protocols often uses cryptographic approaches to prevent unauthorized access and IVN data tampering [13] [14] [15] [16] [17][18]. However, it suffers from the following shortcomings. First, vehicle operations are subject to strict real-time constraints, making high latency and overhead difficult to tolerate. Second, the incompatibility of security enhancement schemes for in-vehicle network protocols requires manufacturers to redesign ECU firmware, incurring significant costs for suppliers when releasing new firmware.

Intrusion detection employs a variety of features, such as the entropy of in-vehicle network[19], message intervals [20], message correlation/consistency [21], ECU fingerprints [22], vehicle voltage [23], communication characteristics [24][25][26]etc., serving as crucial indicators in identifying deviations from normal behavior within the vehicle network. Nevertheless, existing intrusion detection approaches are deployed in IVN and detect anomalies with the stability features of IVN traffic, they cannot identify the injected abnormal messages with normal traffic patterns, especially for time-excitation injection attack. Moreover, most intrusion detection approaches rely on a single type of vehicle data, such as sensor readings, CAN frames, or OBD-II messages, to detect anomalies. This single-source focus limits detection effectiveness, as each method is tailored to a specific data type and cannot easily be applied to others.

To overcome the limitations of existing works, in this paper, we propose a novel model, named MDHP-Net, to detect time-excitation injection attack in IVN. MDHP-Net uses Multi-Dimensional Hawkes Process (MDHP) to profile the abnormal behaviors of attacker, and temporal structure MDHP-LSTM is combined to extract time-excitation features. It is worth noting that, we focus on Ethernet in this

paper, but MDHP-Net can be applied to other IVNs.

It is non-trivial to design MDHP-Net because of two major challenges. **C1: Deriving accurate closed-form solutions for the MDHP remains a challenge, as does the lack of open-source solvers for rapid parameter estimation.** Closed-form solutions are essential for precise modeling of the MDHP, enabling a better representation of the dynamic interactions in sequential events. Open-source solvers are equally crucial, as they facilitate quick parameter estimation, which is vital for real-time applications. **C2: Effectively incorporating attacker behavior characteristics captured by the MDHP into a temporal structure, LSTM, remains challenging.** Current approaches struggle to seamlessly integrate the self-exciting, event-dependent features of the Hawkes process within the LSTM framework, limiting the model’s ability to enhance temporal feature extraction. Addressing this gap is crucial for improving the analysis and prediction of complex attack patterns over time.

In this paper, we leverage novel mathematic modeling and designs to address these challenges. Specifically, to address **C1**, we derive the closed-form of the MDHP function to characterize the dynamic behavior of attackers, and further develop a gradient descent solver tailed for MDHP (4). A set of advanced optimization strategies is used to obtain the optimal MDHP parameters. To deal with **C2**, we propose an injection attack detector that integrate optimal MDHP parameters with a novel structure: MDHP-LSTM to enhance temporal feature extraction (5). We adopt a residual self-attention mechanism to accelerate the temporal model’s convergence and enhance detection accuracy.

We summarize the main contribution as follows:

- We provide a theoretical derivation of time-excitation injection attack based on MDHP. Furthermore, we develop the first open-source gradient descent solver, MDHP-GDS, with cutting-edge optimization strategies, for MDHP parameter estimation to capture the dynamic and exciting properties inherent in the behavior of injection attackers.
- We propose a novel temporal-based deep learning model named MDHP-Net to detect time-excitation injection attacks on IVN. MDHP-Net obtains optimal MDHP parameters embedded in MDHP-LSTM blocks, in order to extract attacker behavior feature, using residual self-attention mechanism to accelerate temporal model’s convergence and enhance detection accuracy. The code of MDHP-GDS and MDHP-Net, the experiment data and the results can all be accessed at: <https://github.com/Tiara8735/MDHP-Net-Anonymous>.
- We conducted extensive experiments to validate the effectiveness of both MDHP-GDS and MDHP-Net. Experimental results indicate that MDHP-GDS achieves high estimation speeds and clearly distinguishes between injection attack scenario distributions. Additionally, MDHP-Net demonstrates robust detection capabilities against injection attacks on IVN, outperforming baseline methods.

## 2. Background

### 2.1. Multi-Dimensional Hawkes Process

Hawkes A.G. [27][28] introduced the concept of Hawkes process and Multi-Dimensional Hawkes process in 1971. The essential property of the Hawkes process is that the occurrence of any event increases the probability of subsequent events occurring. To elucidate the principles of the Hawkes process, several foundational definitions will be introduced below.

**Counting process:** A counting process is a specific type of stochastic process  $\{N(t), t \geq 0\}$  that satisfies the condition where  $N(t)$  denotes the cumulative number of events that have occurred by time  $t$ . Consequently, a counting process  $N(t)$  must satisfy the following criteria [29]:

- I.  $N(t) \geq 0$ ;
- II.  $N(t)$  is integer valued;
- III. If  $u < t$ , then  $N(u) \leq N(t)$ ;
- IV. For  $u < t$ ,  $N(t) - N(u)$  expresses the number of events that have occurred in the interval  $(u, t]$ .

**Intensity function:** The intensity function  $\lambda(t)$ , describes the instantaneous rate at which events occur within a point process. In simple cases, such as the homogeneous Poisson process, this intensity function remains constant [30]. However, many practical applications require a more flexible model, which leads to the concept of the conditional intensity function. The conditional intensity function is more generalized as it takes into account the historical information of the process<sup>2</sup>. Point processes that possess an intensity function and also serve as counting processes are known as regular point processes (RPPs) [31]. The Hawkes process is a prominent example of an RPP, with its intensity function defined as follows [28]:

$$\begin{aligned} \lambda(t) &= \mu + \int_0^t g(t-s) dN(s) \\ &= \mu + \sum_{x^\tau < t} g(t-x^\tau) \end{aligned} \quad (1)$$

where  $\mu$  is the the baseline intensity of the Hawkes process;  $g(t)$  is the excitation function.

In contrast to the Poisson process, the Hawkes process considers the influence of historical events, assuming that past events have a positive impact on the occurrence of present events, exhibiting a characteristic of memory. Typically, the excitation function ( $g(t)$ ) is an exponentially decaying function, reflecting the phenomenon that the influence of an event diminishes over time [32][28]. The excitation function is typically defined as  $\alpha e^{-\beta t}$ . Thus, the intensity function of the Hawkes process is generally represented as [33]:

$$\lambda(t) = \mu + \sum_{x^\tau < t} \alpha e^{-\beta(t-x^\tau)} \quad (2)$$

<sup>2</sup> Some papers exhibit inconsistencies in their use of the terms "intensity function" and "conditional intensity function." In many cases, the term "intensity function" is used for simplicity, and readers are expected to infer from the context that it refers to a conditional intensity function.

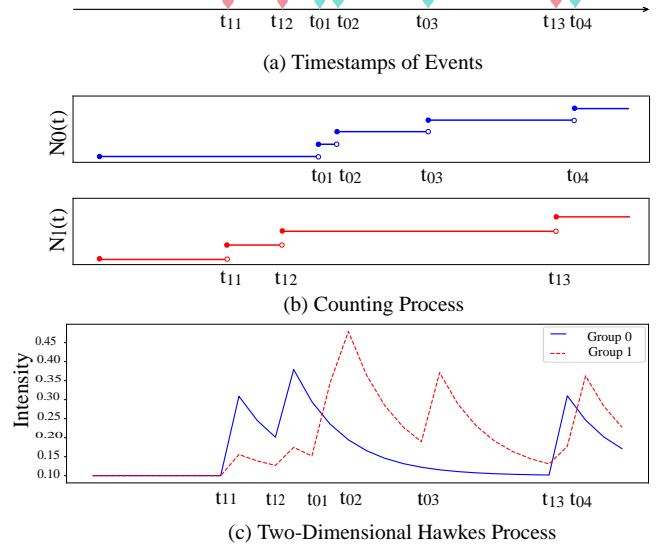


Figure 2: Two-Dimensional Hawkes Process: (a) The occurrence of two types of events within a time interval. (b) The counting process of each event type over time. (c) The intensity function of a bivariate Hawkes process, with parameters  $\theta = [0.1, 0.1]$ ,  $\alpha = \begin{bmatrix} 0 & 0.3 \\ 0.3 & 0.08 \end{bmatrix}$ , and  $\beta = \begin{bmatrix} 0.7 & 0.7 \\ 0.7 & 0.7 \end{bmatrix}$ .

For Multi-Dimensional Hawkes process, we not only consider the self-excitation effect of a single type of event but also the mutually-excitation between different types of events (Figure 2). In a Multi-Dimensional Hawkes process, the intensity function is represented in vector form, rather than as a single mathematical function. Each element of the vector represents the intensity function for the self-excitation of one event and the mutually-excitation between different events. Specifically, the intensity function can be expressed as:

$$\lambda^i(t) = \theta_i + \sum_{j=0}^{D-1} \sum_{k \wedge T_j^k < t} \alpha^{(i,j)} e^{-\beta^{(i,j)}(t-T_j^k)} \quad (3)$$

where

- $\theta_i$  represents the baseline intensity of the Multi-Dimensional Hawkes process, where  $i$  denotes the number of events (equivalent to the number of ECUs).
- $\alpha^{(i,j)}$  represents the amplitude coefficient of the Multi-Dimensional Hawkes process, indicating the positive influence of event  $i$ 's occurrence on event  $j$ .
- $\beta^{(i,j)}$  represents the decay coefficient of the Multi-Dimensional Hawkes process.

### 2.2. Temporal deep-learning model

Temporal deep-learning models are widely used for network attack detection due to their excellent detection accuracy [34][35][36][37]. Common examples of deep temporal

models include Recurrent Neural Networks (RNNs) and Long Short-Term Memory (LSTM) networks.

RNN is a type of traditional temporal structure designed for processing time dependent sequential data [38]. The basic structure of an RNN includes an input layer, a hidden layer, and an output layer. RNN update its internal state by combining the current input with the hidden state from the previous time step, where the hidden state ( $h_t$ ) is computed by Equation 4

$$h_t = f(W_h h_{t-1} + W_x x_t + b) \quad (4)$$

where  $h_t$  is the hidden state at time  $t$ ,  $x_t$  is the input at time  $t$ , and  $b$  is the bias.

LSTM [39] is an optimized variant of RNN. LSTM effectively addresses the challenge of capturing long-term dependencies within sequences, making it particularly suitable for scenarios where messages separated by significant time intervals within a window can substantially influence outcomes [40]. LSTM utilizes gating mechanisms to control the flow of information, thus mitigating the gradient vanishing and exploding problems that are prevalent in RNN.

### 3. Overview

#### 3.1. Threat model

In this paper, we examine a time-exciting injection attack model inspired by patterns observed in real-world network attack data. This type of attack involves injecting abnormal data or messages into the IVN through external entities such as telematics systems, OBD-II ports, T-Boxes, and various sensors. The primary objective of this threat model is to exploit these entry points to compromise the security of IVN systems and achieve specific malicious targets.

**Assumptions:** In this scenario, it is assumed that the attacker has an in-depth understanding of specific messages and data fields within the IVN, including protocols like Ethernet and CAN commonly used in automotive systems. The attacker may obtain physical access to the IVN via the OBD port or connect remotely through an On-Board Unit (OBU). With this level of access, they can observe and transmit packets across the IVN, enabling them to log, recognize, and inject individual messages or sequences of messages. Such intrusions have the potential to interfere with normal vehicle functionality, leading to unexpected malfunctions or prompting the vehicle to perform actions misaligned with its current state.

**Time-exciting injection attacks:** The attacker possesses certain access resources and permissions, allowing them to make repeated attempts to identify vulnerabilities within the system. The likelihood of a successful attack is no longer completely independent of previous attempts. Instead, the cumulative experience gained from past attempts enhances the chances of a successful attack over time. This reflects a temporal accumulation effect, where each attempt affect the probability of success in future attacks.

### 3.2. Detection approach

We propose a time-exciting injection attack detection method, as illustrated in Figure 3. This study profiles abnormal behaviors within the IVN, using the automotive Ethernet protocol SOME/IP as an example to illustrate potential attack scenarios. SOME/IP, a protocol designed for the automotive industry, effectively addresses the limitations of traditional vehicle network technologies (such as CAN bus, MOST, and FlexRay) in terms of bandwidth. However, vulnerabilities often exist in commercial vehicle network stacks, particularly in Bluetooth, Wi-Fi, and 4G modules, significantly increasing the risk of unauthorized remote access to IVN [9][10].

To capture the dynamic behavior of time-exciting injection attacks, we first outline these attack scenarios and provide a precise derivation of closed-form solutions. We then develop an open-source gradient descent solver tailored for MDHP to enable rapid parameter estimation. Finally, we integrate optimal MDHP parameters into MDHP-Net, incorporating key attacker behavior characteristics, which allows us to classify and detect potential attacks accurately.

### 4. MDHP Gradient Descent Solver

#### 4.1. Likelihood

The log-likelihood function for the univariate Hawkes process has been given by T.Ozaki.[33]. For Multi-Dimensional Hawkes processes, we obtained the most comprehensive log-likelihood function through the detailed derivation below. Initially, the likelihood function for Multi-Dimensional Hawkes processes is expressed by a straightforward equation:

$$L = \prod_{i=0}^{D-1} \prod_{t=T_i^{(0)}}^{T_i^{\text{last}}} \lambda^i(t) \cdot e^{-\int_0^{T_{\text{span}}} \lambda^i(v) dv} \quad (5)$$

Where  $\lambda^i(t)$  is the intensity function of each ECU. The full derivation is given in Appendix 10.1. The likelihood function is further transformed into the log-likelihood:

$$\ln L = \sum_{i=0}^{D-1} \sum_{t=T_i^{(0)}}^{T_i^{\text{last}}} \ln \left( \theta_i + \sum_{j=0}^{D-1} \sum_{k:T_j^k < t} \alpha^{(i,j)} e^{-\beta^{(i,j)}(t-T_j^k)} \right) - \underbrace{\sum_{i=0}^{D-1} \int_0^{T_{\text{span}}} \left( \theta_i + \sum_{j=0}^{D-1} \sum_{k:T_j^k < v} \alpha^{(i,j)} e^{-\beta^{(i,j)}(v-T_j^k)} \right) dv}_{\text{call this } \Gamma} \quad (6)$$

In fact,  $\Gamma$  is a computable function. Therefore, we further simplify the expression to obtain a more accurate log-likelihood function, as shown in Equation 7. The full derivation is given in Appendix 10.2.

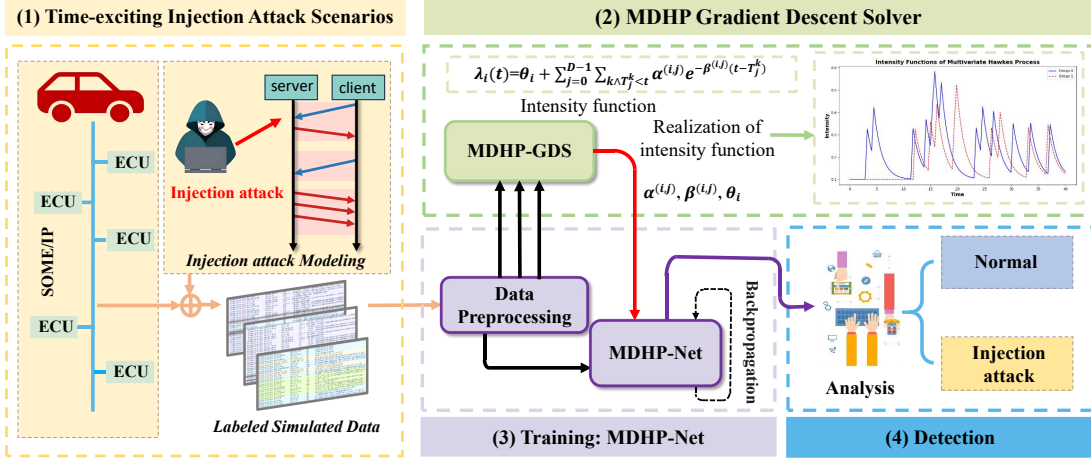


Figure 3: The detection framework for time-exciting injection attacks. It presents a detection framework for time-exciting injection attacks on in-vehicle networks. It consists of four parts: (1) modeling of injection attack scenarios, (2) the MDHP Gradient Descent Solver for calculating intensity functions, (3) training of the MDHP-Net, and (4) detection of normal versus injection attack patterns. The dataset uses the automotive Ethernet protocol SOME/IP to illustrate potential attack scenarios.

$$\ln L = \sum_{i=0}^{D-1} \sum_{t=T_i^{(0)}}^{T_i^{\text{last}}} \ln \left( \theta_i + \sum_{j=0}^{D-1} \sum_{k \wedge T_j^k < t} \alpha^{(i,j)} e^{-\beta^{(i,j)}(t-T_j^k)} \right) - T_{\text{span}} \sum_{i=0}^{D-1} \theta_i + \sum_{i=0}^{D-1} \sum_{j=0}^{D-1} \left( \frac{\alpha^{(i,j)}}{\beta^{(i,j)}} \sum_k \left( e^{-\beta^{(i,j)}(T_{\text{span}}-T_j^{(k)})} - 1 \right) \right) \quad (7)$$

where

$D$  = MDHP Dim, i.e., Number of ECUs

$T_i^{(k)}$  = Timestamp of the  $k^{\text{th}}$  message sent by the  $i^{\text{th}}$  ECU

$T_{\text{span}}$  = Time span of the observation window

$\alpha, \beta, \theta$  = Hawkes parameters;

Both  $\alpha$  and  $\beta$  are  $(D, D)$  matrices,

and  $\theta$  is a  $(D)$  vector.

## 4.2. The Design of MDHP-GDS

We develop a gradient descent solver specifically tailored for the Multi-Dimensional Hawkes Process (MDHP-GDS)<sup>3</sup>, aimed at accurately estimating optimal MDHP parameters from given data samples.

MDHP-GDS is implemented entirely in Python and utilizes PyTorch's Autograd feature extensively [41]. Auto-

grad simplifies the process of automatic differentiation by constructing a computational graph from the loss function, applying the chain rule to compute gradients, and updating the parameters accordingly. For our specific application, the parameters to be updated are  $\alpha, \beta$  and  $\theta$ , using the negative log-likelihood  $(-\ln L)$  as the loss function in Equation 7.

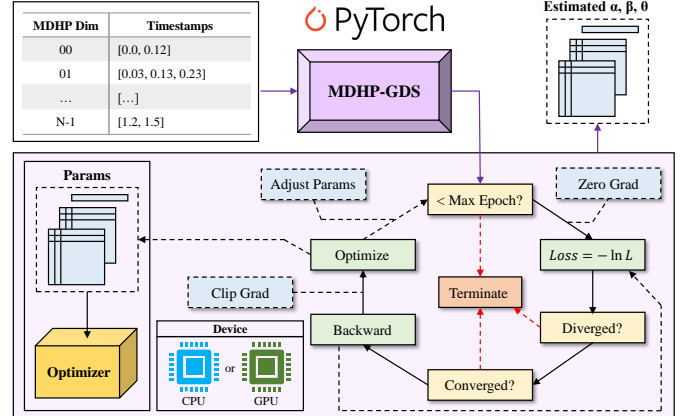


Figure 4: Workflow of MDHP-GDS

The workflow of MDHP-GDS is depicted in Figure 4. The solver contains three tensors, two of shape  $(\text{dim}, \text{dim})$ , and one of shape  $(\text{dim})$ , respectively representing the parameters  $\alpha, \beta$  and  $\theta$ . These tensors are Autograd-enabled, allowing them to be learnable parameters that can be optimized using a PyTorch optimizer; In our experiments, we selected Adam [42] for this purpose. Moreover, based on the scale of the problem, both CPU and GPU are supported for the calculation.

The optimization cycle is meticulously orchestrated, which begins by clearing the accumulated gradients from

3. We provide a comprehensive Jupyter notebook at the following link: <https://github.com/Tiara8735/MDHP-Net-Anonymous/blob/main/examples/MDHP-GDS.ipynb>, which demonstrates the usage of MDHP-GDS in detail. By reviewing this notebook alongside the corresponding source code, researchers can gain a clearer understanding of the design and structure of MDHP-GDS.

the previous epoch to prevent convergence failure. Following this, the loss is calculated based on Equation 7. The state of the solver is then assessed against a predefined threshold to determine whether to halt the gradient descent process in advance. Subsequent steps involve the backward propagation and optimization to adjust the learnable parameters. To safeguard against potential issues such as vanishing or exploding gradients, we incorporate a gradient clipping operation and parameter adjustments at the end of each epoch.

### 4.3. Optimization

Calculating the loss function constitutes the most time-consuming part of the gradient descent procedure, and the complex loop structure of Equation 7 presents a more severe challenge for fast parameter-estimation speed. Therefore, in the context of in-vehicle communications, where vast quantities of data are transmitted each millisecond, it is crucial to implement a well-conceived optimization strategy for loss calculation in each epoch.

In general, MDHP-GDS incorporates advanced optimization techniques such as: 1. Padding and Masking; 2. Computational Decoupling; 3. Vectorization; 4. GPU Offloading. 5. Just-In-Time (JIT) Compilation. These methods enhance computational efficiency, and the correlated algorithms are detailed in Appendix 10.3.

## 5. MDHP-NET: The Proposed Model

### 5.1. Overall Structure

Figure 5 depicts the process of model forwarding, designed for the analysis of  $n$  time-stamped messages within a detection window to perform multiple classification tasks. Within our SOME/IP data described in Section 6.1.2, each message is characterized by 10 specific message fields plus a temporal attribute.

### 5.2. Preprocess

During preprocessing, discrete message fields in the SOME/IP messages (including Message Type and Error Code) undergo one-hot encoding to generate binary vector representations. This encoding facilitates the network's ability to capture relationships between discrete categorical values. Furthermore, we restructure the input tensor dimension from  $(batch\_size, \dots)$  to  $(n\_seq, \dots)$  to enable later parallel processing of sequential data in the MDHP-LSTM layers, where  $n\_seq$  represents the number of messages in each window.

### 5.3. SMB

Following the initial preprocessing, we implement a Sequence Mapping Block (SMB) to enhance feature representation. The SMB employs learnable affine transformations defined as  $A(m) = Wm + b$ , to project each message

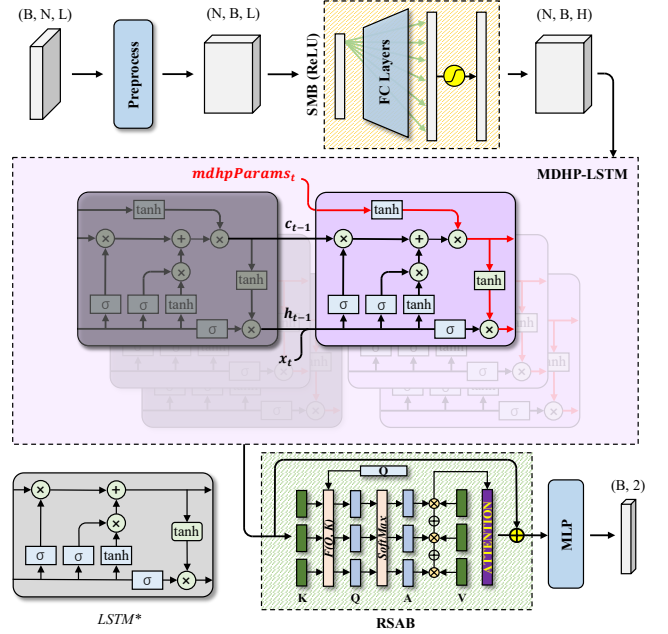


Figure 5: The Overall Structure of MDHP-Net. **B**: Batch Size. **N**: Number of Sequences per Window. **L**: Length of Each Sequence. **H**: Hidden Size. \*LSTM is not used in MDHP-Net, shown here only for comparison with MDHP-LSTM.

into a higher-dimensional feature space. A ReLU activation function is subsequently applied to capture non-linear relationships in the data. Moreover, SMB incorporates flexible dimension transformation operations to accommodate varying input requirements of different models.

### 5.4. MDHP-LSTM

Traditional LSTM architectures, while effective at capturing temporal dependencies, lack the explicit modeling of event excitation and decay patterns characteristic of cyber attacks. This limitation becomes particularly significant in injection attack detection, where the temporal intensity of events carries crucial discriminative information.

To address this limitation, we propose MDHP-LSTM, which augments the standard LSTM architecture with MDHP parameters as shown in Equation 8:

$$\begin{aligned}
 \mathbf{i}^t &\leftarrow \sigma(\mathbf{W}_i \mathbf{x}^{t-1} + \mathbf{U}_i \mathbf{h}^{t-1} + \mathbf{b}_i) \\
 \mathbf{f}^t &\leftarrow \sigma(\mathbf{W}_f \mathbf{x}^{t-1} + \mathbf{U}_f \mathbf{h}^{t-1} + \mathbf{b}_f) \\
 \mathbf{hks}^t &\leftarrow \tanh(\mathbf{A}\alpha^x - \mathbf{B}(\beta^x \mathbf{T}_{span}^x) + \mathbf{C}\theta^x) \\
 \tilde{\mathbf{c}}^t &\leftarrow \tanh(\mathbf{W}_c \mathbf{x}^{t-1} + \mathbf{U}_c \mathbf{h}^{t-1} + \mathbf{b}_c) \\
 \mathbf{c}^t &\leftarrow \mathbf{hks}^t * (\mathbf{f}^t * \mathbf{c}^{t-1} + \mathbf{i}^t * \tilde{\mathbf{c}}^t) \\
 \mathbf{o}^t &\leftarrow \sigma(\mathbf{W}_o \mathbf{x}^{t-1} + \mathbf{U}_o \mathbf{h}^{t-1} + \mathbf{b}_o) \\
 \mathbf{h}^t &\leftarrow \mathbf{o}^t * \tanh(\mathbf{c}^t) \\
 \mathbf{y}^t &\leftarrow \mathbf{W}_y \mathbf{h}^{t-1}
 \end{aligned} \tag{8}$$

where  $\alpha^x$ ,  $\beta^x$ , and  $\theta^x$  represent the excitation, decay, and baseline intensity parameters of the Multi-Dimensional Hawkes process, respectively. The matrices **A**, **B**, and **C** learn to map these parameters to the module’s internal state space.

The Hawkes state modulates both the cell state  $\mathbf{c}^t$  and hidden state  $\mathbf{h}^t$  through multiplicative interactions, as illustrated by the red paths in Figure 5. This integration allows the network to adaptively adjust its memory based on the temporal intensity patterns captured by the Hawkes process parameters, providing a more nuanced representation of attack dynamics.

## 5.5. RSAB

The RSAB enhances the detection of coordinated intrusion attacks by capturing temporal dependencies across message sequences. While individual messages in an attack sequence may appear legitimate, the attention mechanism learns to identify suspicious patterns by computing contextual weights across the temporal window.

Mathematically, the attention mechanism within the RSAB can be expressed as:

$$\text{Attention}(x) = \text{Softmax} \left( \frac{QK^T}{\sqrt{d_k}} \right) V \quad (9)$$

where  $Q$ ,  $K$ , and  $V$  are the query, key, and value matrices derived from the input data  $x$ , and  $d_k$  is the scaling factor corresponding to the dimension of the keys. This attention function allows the network to prioritize certain messages within a window, which is crucial when a single malicious packet could indicate a potential attack.

The residual connections in RSAB enable efficient gradient propagation during back-propagation, addressing the vanishing gradient problem inherent in deep neural architectures:

$$\text{RSAB}(x) = x + \text{Attention}(Q, K, V) \quad (10)$$

This design is particularly effective for SOME/IP traffic analysis, where discriminative features may be embedded deep within the temporal sequences.

## 5.6. MLP

The final output of MDHP-Net models passes through a Multi-Layer Perceptron (MLP) block, becoming a tensor with the shape of (2), indicating the probability of the input window being normal or suffering from intrusion attacks.

# 6. Experiment

## 6.1. Overview

**6.1.1. Setup.** The hardware and software specifications of the experiments are detailed in Tables 2 and 3, respectively.

Table 2: Device Specification

Device	Model Name	Number
CPU	Intel Xeon Silver 4210 CPU @ 2.20 GHz	1
GPU	NVIDIA GeForce RTX 3090 (24GB DRAM)	2*

Table 3: Software Specification

Software	Version
System	Ubuntu 22.04.5 LTS
Python	3.12.4
PyTorch	2.4.0

\*Dual GPUs are utilized for training MDHP-Net and baseline models, while single GPU configuration is employed for MDHP parameter estimation via MDHP-GDS and model inference.

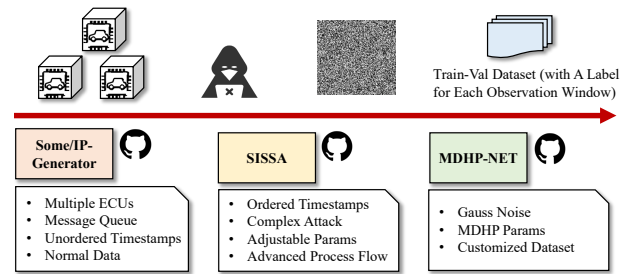


Figure 6: Dataset Generation Process.

**6.1.2. Dataset.** As depicted in Figure 6, the generation of SOME/IP message data in our experiment utilizes a suite of GitHub open-source tools, including the SOME/IP-Generator<sup>4</sup>, SISSA<sup>5</sup>, and MDHP-NET<sup>6</sup>. These tools orchestrate the data generation process from multiple dimensions, ensuring the data aligns with real-world scenarios. This alignment facilitates the production of high-quality data streams, representing both typical vehicle communication traffic and traffic under injection attack conditions.

**SOME/IP-Generator:** The SOME/IP-Generator, a Python-based tool for generating Some/IP packets, is openly available on GitHub and commonly adopted in intrusion detection research [26][43]. This generator utilizes Python’s multiprocessing features and multiple communication queues to effectively emulate the dynamic exchange of Some/IP packets among various ECUs within a Local Area Network (LAN) over extended periods. However, the repository’s lack of recent updates limits its adaptability to modern, complex message behaviors, particularly in scenarios that demand strict real-time compliance, thereby reducing its effectiveness in simulating time-sensitive attack scenarios.

**SISSA:** SISSA [43] builds on Some/IP-Generator by creating a corpus of standard Some/IP data, which is then processed into discrete segments. These segments are random-

4. [https://github.com/Egomania/SOME-IP\\_Generator](https://github.com/Egomania/SOME-IP_Generator)

5. <https://github.com/jamesnulliu/SISSA>

6. <https://github.com/Tiara8735/MDHP-Net-Anonymous/tree/main>

ized, split into uniform windows, and sorted into buckets for classification tasks. SISSA adds adjustable parameters for increased realism and data robustness, as detailed in Table 4, where four random ECUs are selected as injection sources, with a 40% chance to inject a message.

Table 4: Parameters of Attack Simulation

Parameter	Value
Injection Rate	0.4
Num of Injection Sources (Each Attack)	4

**MDHP-Net** After generating both the normal and abnormal in-car traffic through SISSA, MDHP-NET applies further in-depth processing to enhance the dataset’s alignment with real-world scenarios. Specifically, we design `SomeIP_MDHP_Dataset` to encapsulate the data uniformly, introduce Gaussian noise to each window, and incorporate support for handling MDHP parameters. These modifications are crucial for refining the dataset, thus facilitating more effective model training and inference processes.

The dataset composition for training and evaluation is presented in Table 5. We constructed a balanced dataset comprising 19,580 windows, each containing 128 SOME/IP messages. The dataset was randomly partitioned into training and validation sets with an 80:20 split, maintaining equal proportions of normal and attack windows to prevent class imbalance. The model weights were frozen after training, and no validation set data was used for model fine-tuning, ensuring unbiased evaluation of the model’s performance. A more detailed description of the dataset is provided in Appendix 10.4.

Table 5: Detailed Information of Training Dataset and Validation Dataset

Window Type	Train Set (msg)	Val Set (msg)
Normal	7832*128	1958*128
Attack	7832*128	1958*128
Sum	15664*128 (80%)	3916*128 (20%)

**6.1.3. Evaluation baselines and metrics.** To rigorously evaluate the proposed MDHP-GDS and MDHP-LSTM, we meticulously crafted a series of experiments tailored to their specific frameworks to confirm their efficacy.

In Section 6.2, we conduct a thorough examination of the estimation speed of MDHP parameters by varying the input data size sent to MDHP-GDS. We executed identical tests on both CPUs and GPUs, demonstrating that our optimizations significantly enhance GPU performance for parameter estimation in large datasets.

In Section 6.3, we present evaluations of MDHP-GDS using our simulated SOME/IP communication messages. We employed the Cumulative Distribution Function (CDF) as a visual metric. The CDF, being the integral of the probability density function, encapsulates the probability distribution of a random variable  $X$ . It is defined for random variable  $X$  in Equation 11:

$$F_X(x) = P(X \leq x) \quad (11)$$

where  $F_X(x)$  represents the probability that the random variable  $X$  assumes a value less than or equal to  $x$ . The probability of  $X$  falling within the semi-closed interval  $(a, b]$  is given in Equation 12.

$$P(a < X \leq b) = F_X(b) - F_X(a) \quad (12)$$

During these experiments, we observed noteworthy differences in CDF outcomes between normal and abnormal communication messages when using MDHP-GDS-estimated parameters. This led us to conclude that MDHP parameters could serve as a robust supplementary feature to enhance the learning capabilities of MDHP-NET.

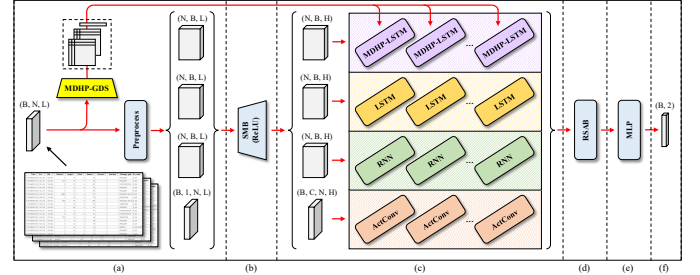


Figure 7: Contrast and Ablation Experiment of MDHP-Net. We compared four different models, MDHP-Net, SISSA-LSTM, SISSA-RNN and SISSA-CNN, by keeping (a), (b), (d), (e) and (f) the same, while changing the backbone blocks in (c). Moreover, MDHP-Net (with MDHP-LSTM blocks) and SISSA-LSTM (with LSTM blocks) comprise the ablation experiment on MDHP parameters.

In Section 6.4, we designed extensive comparative and ablation experiments to demonstrate the significant advantages of MDHP-Net in detecting injection attacks on in-vehicle SOME/IP communication messages. As illustrated in Figure 7, we compared MDHP-Net with three models with different architectures proposed in SISSA[43]. To ensure the fairness of the experiments, we maintained the overall structure of the models while replacing the key module in Figure 7-(c) with multiple MDHP-LSTM blocks to complete the construction of MDHP-Net. In general, we aimed to compare MDHP-Net with SISSA-LSTM, SISSA-RNN, and SISSA-CNN under conditions that ensure as much fairness as possible.

## 6.2. MDHP-GDS: Estimation Speed

In Section 4.3, we have presented comprehensive optimizations for the parameter estimation process of MDHP-GDS, primarily focusing on gradient descent optimization for the negative log-likelihood function. We evaluate the MDHP-GDS parameters using two quantitative metrics:

- **Window Time:** Seconds spent for estimating the MDHP parameters for one window in average.
- **Throughput:** Number of messages MDHP-GDS can handle per second. In our experiment, number of messages is randomly generated according to the test configurations but recorded precisely after generation.



For experimental reproducibility, we set the Random Seed to 2024 and enable both `torch.compile` and optimized log-likelihood computation.

As mentioned in previous sections, `torch.compile` implements Just-In-Time (JIT) compilation and kernel-fusion instead of interpreted execution, which is consistently enabled being fair across all experiments. The optimized log-likelihood computation is crucial, as the unoptimized version exhibits prohibitive computational overhead even for small-scale datasets (e.g., with MDHP dimension of 5, maximum timestamp length of 10 and minimum of 5, parameter estimation for a single window requires 28.5 seconds in CPU mode and 70.3 seconds in GPU mode; This is 98% slower than the optimized one on CPU and 99% slower on GPU). Nevertheless, an unoptimized log-likelihood implementation is still provided in the source code of MDHP-GDS <sup>7</sup>, allowing interested researchers to conduct further tests by easily altering the configuration files as needed.

Table 6: Estimation Speed of MDHP-GDS with CPU.

Dim	Max-T-Len	Min-T-Len	Window-Cost	Throughput
5	10	5	0.3144	4.3255
10	100	50	0.4988	61.7397
15	100	50	0.5982	74.6160
20	100	50	0.6896	88.7971
25	100	50	0.9819	72.8373
30	100	50	1.3888	61.5767
30	150	50	2.0903	61.3496
30	200	50	3.4459	42.4848

Table 6 presents the parameter estimation performance of MDHP-GDS in CPU mode. The results demonstrate that as the input scale increases, the Window-Cost exhibits a clear upward trend, while Throughput peaks at 88.7971 packets per second before declining. This performance characteristic can be attributed to our optimization algorithm’s efficient utilization of CPU vector operations and parallel processing capabilities. However, the physical core limitations become apparent when processing high-dimensional matrix operations on large datasets. Furthermore, the computational overhead increases due to the masking operations required for padded elements. However, CPU mode remains efficient for small-scale datasets in deed.

Table 7: Estimation Speed of MDHP-GDS with GPU.

Dim	Max-T-Len	Min-T-Len	Window-Cost	Throughput
5	10	5	0.4079	3.3335
10	100	50	0.5710	53.9324
15	100	50	0.4807	92.8501
20	100	50	0.3383	181.0082
25	100	50	0.3902	183.2755
30	100	50	0.3471	246.3298
30	150	50	0.3173	404.0592
30	200	50	0.3469	421.9364

Table 7 illustrates the parameter estimation performance of MDHP-GDS in GPU mode. While GPU mode shows marginally lower performance than CPU mode for small-scale datasets, it demonstrates superior scalability as data

dimensions and timestamp volumes increase. Despite the growing computational complexity from increased masking operations and timestamp variance per MDHP dimension, the GPU implementation maintains stable Window-Cost metrics and exhibits consistent Throughput improvement, exceeding 400 messages per second in our largest test cases. This superior scaling behavior can be attributed to the synergy between our vectorized computation optimizations and the GPU’s massive parallel threading architecture. For high-dimensional Hawkes process parameter estimation tasks, we recommend the GPU implementation of MDHP-GDS for optimal estimation performance.

### 6.3. MDHP-GDS: Estimation Results

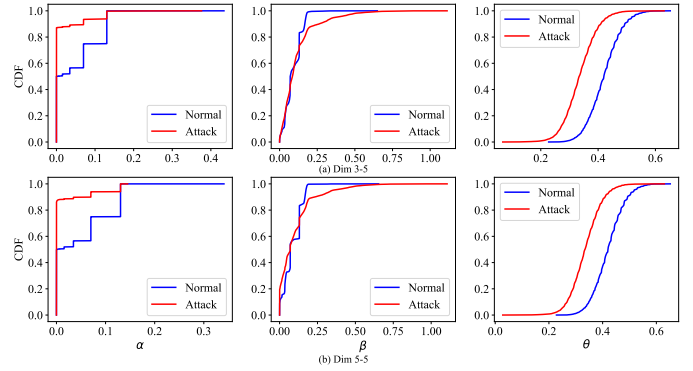


Figure 8: CDF of (a) Dim 3-5 and (b) Dim 5-5.

We evaluated the MDHP parameter estimation performance of our MDHP-GDS framework using simulated SOME/IP communication data. For each temporal window, the MDHP parameters consist of three components: the excitation matrix  $\alpha \in \mathbf{R}^{Dim \times Dim}$ , the decay matrix  $\beta \in \mathbf{R}^{Dim \times Dim}$ , and the baseline intensity vector  $\theta \in \mathbf{R}^{Dim}$ , where  $Dim$  denotes the number of ECUs in the system.

In our simulated SOME/IP attack dataset, attackers randomly select source IP addresses from legitimate ECUs for packet injection. Therefore, any individual ECU has a probability of  $1/Dim$  of being selected as the injection source, and  $(Dim - 1)/Dim$  of not being selected.

Figure 8 illustrate the CDF plots for two representative inter-ECU communications: Dim 3-5 (communication from ECU 3 to ECU 5) and Dim 5-5 (self-exciting process of ECU 5). The analysis reveals distinct parameter distributions between normal and attack scenarios, providing discriminative features for the subsequent deep learning process:

- 1) Excitation Matrix ( $\alpha$ ): Attack windows demonstrate a leftward shift in CDF curves for both Dim 3-5 and Dim 5-5 scenarios. This shift indicates reduced excitation values during attacks, as ECU 3 is statistically less likely to be selected as the injection source. During attacks, windows contain more injected packets with randomly selected source IPs, resulting in weaker self-excitation processes for individual ECUs like ECU 3.

<sup>7</sup> [https://github.com/Tiara8735/MDHP-Net-Anonymous/blob/main/mdhpnets/models/mdhp\\_gds.py#L298-L333](https://github.com/Tiara8735/MDHP-Net-Anonymous/blob/main/mdhpnets/models/mdhp_gds.py#L298-L333)

- 2) Decay Matrix ( $\beta$ ): Attack conditions exhibit higher decay rates, indicating faster attenuation of previous events' influence. This property reflects reduced temporal dependencies between legitimate SOME/IP messages during attacks. The increased  $\beta$  values for ECU 3 and ECU 5 correlate with their statistical unlikelihood of being selected as injection sources.
- 3) Baseline Intensity ( $\theta$ ): Attack scenarios show consistently lower baseline intensity values for non-attacking ECUs. This reduction occurs because attacker-controlled ECUs transmit at higher intensities, causing a compensatory decrease in the baseline intensity of legitimate communications (such as Dim 3-5 and Dim 5-5) within the observation window.

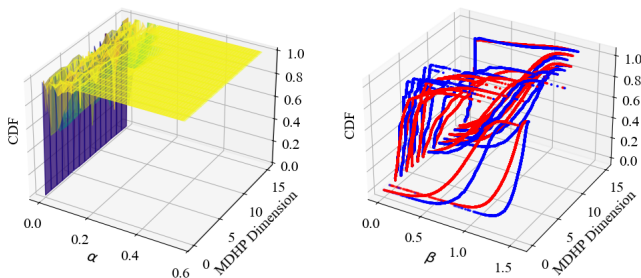


Figure 9: 3D Visualization of CDF Dim 5.

Figure 9 presents three-dimensional CDF visualizations for  $\alpha$  and  $\beta$ , focusing on interactions between all ECUs and ECU 5. The 3D representations reveal distinct distributional patterns between normal and attack states. The left subplot displays the excitation matrix ( $\alpha$ ) CDF distribution, while the right subplot shows the decay matrix ( $\beta$ ) CDF distribution, both exhibiting clear topological differences between attack and normal states. More experiment results of different dimension are shown in Appendix 10.5.

These distinctive parameter distributions quantify the temporal perturbations in SOME/IP communication patterns during injection attacks. The clear separability between normal and attack distributions validates our approach and motivates our proposed MDHP-Net architecture, which leverages these temporal dynamics for attack detection. The ability to capture fine-grained differences in inter-ECU communication patterns through MDHP parameter estimation provides a robust foundation for automotive network intrusion detection.

## 6.4. MDHP-Net: Contrast and Ablation Experiment

**6.4.1. Performance in Training.** Figure 10 illustrates the comparative training dynamics of MDHP-Net against baseline models. In subfigures (a) and (b), MDHP-Net, SISSA-RNN, and SISSA-LSTM demonstrate rapid initial loss reduction on the training set, indicating effective feature capture from the SOME/IP message windows. MDHP-Net exhibits notably faster convergence. In contrast, subfigure (c)

shows that SISSA-CNN, despite consuming 20 $\times$  more memory during inference, displays slower initial training loss reduction with even greater learning rate. This performance difference underscores the effectiveness of temporal feature modeling for injection attack detection compared to spatial (CNN-based) approaches.

During epochs 40-50, while SISSA-RNN and SISSA-LSTM achieve 0.99 accuracy on the training set, their validation set performance remains substantially lower, indicating non-negligible overfitting. MDHP-Net demonstrates better generalization, with closer alignment between training and validation accuracies, suggesting enhanced model robustness. We attribute this improved performance to the MDHP parameters providing meaningful temporal feature information during inference, enabling better discrimination between normal and anomalous patterns, which aligns with our initial hypothesis.

The experimental results demonstrate MDHP-Net's superior performance across several metrics:

- Faster convergence compared to SISSA-LSTM and SISSA-RNN.
- Enhanced training stability.
- Superior validation set performance - Highest validation accuracy of MDHP-Net: 0.9906; of SISSA-LSTM: 0.9839; of SISSA-RNN: 0.9750.
- While SISA-CNN achieves high training accuracy, its significant underfitting on the validation set indicates inadequate temporal feature capture, confirming the superiority of temporal neural architectures for this specific intrusion detection scenario.

Table 8 presents the training hyperparameters. To ensure reproducibility in our distributed training setup using `torch.DistributedDataParallel`, we initialized the random seed as 1024 + RANK, where RANK represents the process identifier. For MDHP-Net and sequence-based models (SISA-LSTM, SISA-RNN), we employed lower learning rate and weight decay values ( $5e^{-5}$ ), while SISA-CNN required higher values ( $3e^{-4}$ ) to achieve effective feature learning.

Table 8: Hyperparameters of Training

Hyperparameter	Value
Random Seed	1024 + RANK_ID
Max Epoch	50
Optimizer	AdamW
Learning Rate	$5e^{-5}$ / $3e^{-4}$
Weight Decay	$5e^{-5}$ / $3e^{-4}$

**6.4.2. Metrics.** Figure 11 presents a comparative performance evaluation of the proposed MDHP-Net against three baseline models (SISSA-CNN, SISSA-RNN, and SISSA-LSTM) using standard metrics: accuracy, precision, recall, and F1-score. MDHP-Net demonstrates superior performance across all metrics, achieving improvements of approximately 3-5 percentage points over the baseline models. This enhancement can be attributed to the MDHP-LSTM module, which incorporates MDHP parameters to

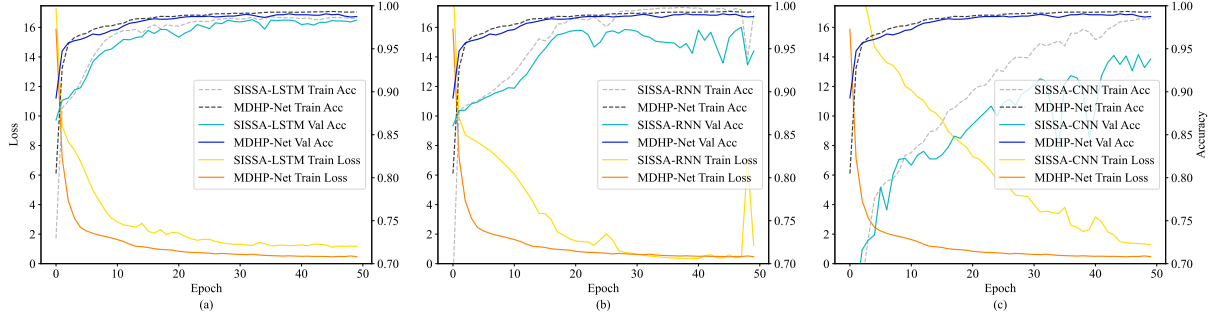


Figure 10: Train, Val Accuracy and Train Loss of MDHP-Net Compared with (a) SISSA-LSTM, (b) SISSA-RNN, (c) SISSA-CNN

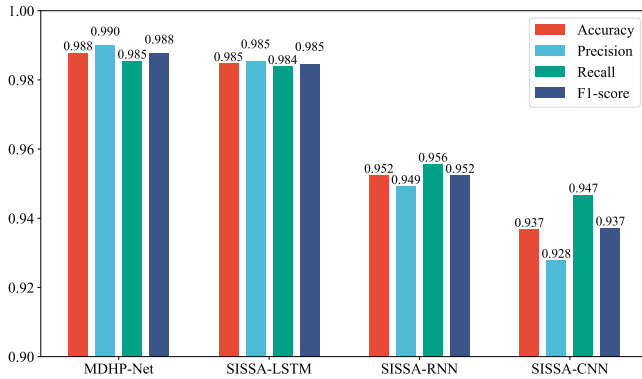


Figure 11: Comparison of Metrics

model both excitation and decay patterns in the temporal domain. The integration of these parameters enables more comprehensive temporal feature extraction compared to conventional LSTM architectures. While SISSA-LSTM shows competitive performance, the CNN and RNN-based variants exhibit limitations in capturing the temporal dynamics of injection attacks. These empirical results validate the effectiveness of incorporating MDHP parameters in the detection of SOME/IP intrusion attacks.

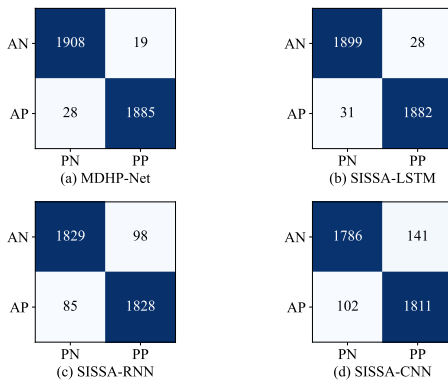


Figure 12: Comparison of Confusion Matrix

Figure 12 presents the confusion matrices for MDHP-Net and the baseline models. MDHP-Net achieves the highest true positive rate ( $1885/1913 \approx 98.5\%$ ) and true negative rate ( $1908/1927 \approx 99.0\%$ ), with minimal false positives (28) and false negatives (19). SISSA-LSTM demonstrates comparable performance, while SISSA-RNN and SISSA-CNN show gradually increasing misclassifications. MDHP-Net's superior performance is particularly evident in its lower false positive rate (1.5%) compared to SISSA-CNN (5.3%), which is crucial for practical deployment in vehicular networks where false alarms could trigger unnecessary defensive measures. All models maintain detection rates above 90%, though MDHP-Net's integration of MDHP parameters provides a marginal but significant advantage in discrimination accuracy.

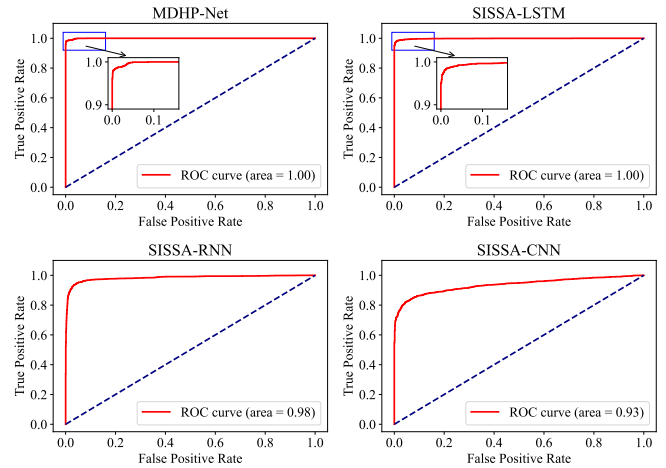


Figure 13: ROC and AUC of Different Models

Figure 13 presents the ROC curves and corresponding AUC metrics for all models. MDHP-Net and SISSA-LSTM achieve optimal AUC scores of 1.00, demonstrating perfect discriminative capability across all classification thresholds. The magnified inset of their ROC curves in the low false positive rate region (0-0.1) reveals consistently high true positive rates, crucial for practical deployment where false alarms must be minimized. SISSA-RNN and SISSA-CNN

exhibit slightly lower performance with AUC values of 0.98 and 0.93, respectively. Their ROC curves show greater deviation from the ideal upper-left corner, particularly in the low false positive rate regime. SISSA-CNN’s more gradual curve slope indicates reduced sensitivity to threshold selection, potentially requiring more careful calibration in deployment scenarios.

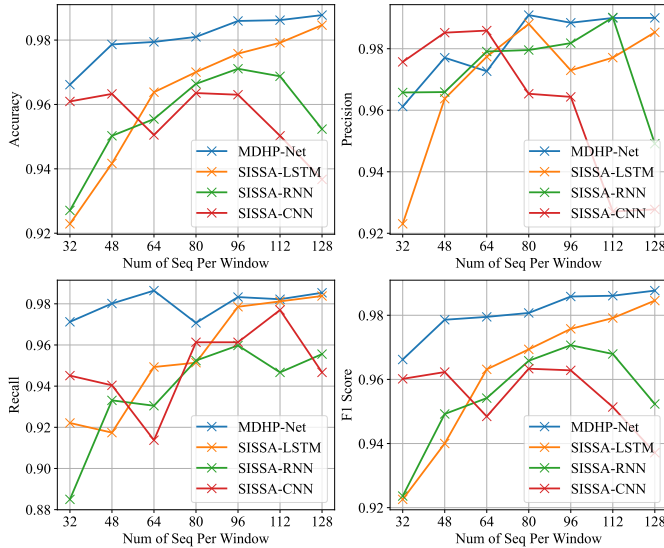


Figure 14: Comparison of Different Numbers of Sequences per Window

Figure 14 illustrates the impact of observation window size on model performance across four metrics. MDHP-Net consistently outperforms the baseline models, maintaining superior performance across different window sizes (32-128 packets). Both MDHP-Net and SISSA-LSTM exhibit monotonic improvement in precision, recall, and F1-score as the window size increases, achieving peak performance at 128 packets. This trend aligns with the theoretical advantages of LSTM architectures in leveraging extended temporal dependencies.

In contrast, SISSA-RNN and SISSA-CNN display non-monotonic performance patterns, with optimal metrics achieved at intermediate or smaller window sizes. Their performance degradation at larger window sizes (>112 packets) suggests limitations in handling increased temporal complexity, stemming from the architectural constraints of RNNs and CNNs in managing long-range dependencies and filtering relevant features from noise over extended time periods.

These results empirically validate that MDHP-Net’s integration of Hawkes process parameters enables more robust feature extraction across varying temporal scales, particularly benefiting from larger observation windows without suffering from the performance saturation observed in traditional architectures.

**6.4.3. Computational Cost Analysis.** Table 9 presents a comparative analysis of model complexity and computa-

tional requirements. MDHP-Net has approximately 5.5% more parameters (2.55M) than SISSA-LSTM (2.41M) due to the additional Hawkes process components. Despite this increased parametric complexity, MDHP-Net maintains comparable memory efficiency, requiring only 18.6% more total memory (113.03MB vs. 95.32MB) than SISSA-LSTM.

SISSA-CNN, while having the smallest parameter count (303K), demonstrates significantly higher computational overhead with a forward/backward pass size of 2839.68MB - approximately 28 times larger than MDHP-Net (100.80MB). This substantial difference stems from the dense convolution operations required for high-dimensional feature extraction. In contrast, the sequence-based architectures (MDHP-Net, SISSA-RNN, and SISSA-LSTM) exhibit more efficient memory utilization due to their sequential processing nature.

The memory footprint analysis reveals that MDHP-Net achieves superior detection performance without incurring prohibitive computational costs. The marginal increase in resource requirements compared to baseline LSTM and RNN models is justified by the significant performance improvements demonstrated in previous experiments.

## 7. Discussion

### 7.1. Further Optimization of MDHP-GDS

While our current implementation achieves significant speedup through vectorization and GPU acceleration, several optimization avenues remain:

- **Batch Processing:** The current gradient solver processes individual observation windows sequentially. Implementing batch processing through tensor padding and alignment could better utilize GPU parallel processing capabilities and memory bandwidth, potentially yielding substantial throughput improvements.
- **Low-level Implementation:** Despite leveraging PyTorch’s JIT compilation and vectorized operations, the Python-based implementation introduces inherent overhead. Reimplementing the core solver in C++ with custom CUDA kernels could significantly reduce computational latency and memory access patterns, particularly for the gradient computation steps.

### 7.2. Architectural Design Considerations

While Transformer architectures have demonstrated remarkable success in NLP and computer vision tasks, their application to intrusion detection systems presents practical challenges. The quadratic complexity of self-attention mechanisms with respect to sequence length and the substantial memory requirements make them suboptimal for real-time network security applications.

MDHP-Net’s architecture prioritizes computational efficiency while maintaining high detection accuracy through targeted feature extraction. The combination of lightweight MDHP-LSTM blocks with a single RSAB module achieves an optimal balance between model expressiveness and resource utilization. This design philosophy aligns with the

Table 9: Computational Cost of Different Models

Model	MDHP-Net	SISSA-LSTM	SISSA-RNN	SISSA-CNN
Total Params	2548738	2414594	2216450	303459
Input Size (MB)	2.04	1.64	1.64	1.64
Forward/Backward Pass Size (MB)	100.80	84.02	84.02	2839.68
Params Size (MB)	10.19	9.66	8.87	1.21
Estimated Total Size (MB)	113.03	95.32	94.52	2842.53

constraints of embedded systems and real-time detection requirements in vehicular networks.

## 8. Related work

**Injection attack detection for CAVs.** The current focus is on detecting and mitigating various data injection attacks targeting connected vehicles, particularly emphasizing the security of the CAN and in-vehicle communication systems. Ben et.al [44] evaluates multiple CAN bus attack detection methods, highlighting the effectiveness of Pearson correlation and noting the high false positive rates associated with unsupervised learning techniques, thereby underscoring the importance of incorporating knowledge about ECU collaboration. Building upon this foundation, Ji et.al [45] introduce an enhanced CNN algorithm designed to detect abnormal data in in-vehicle networks, effectively addressing high false negative rates through the utilization of data field characteristics and Hamming distance. Jedh et.al [46] propose a method that utilizes message sequence graphs and cosine similarity to enhance real-time cybersecurity against message injection attacks on the CAN bus. Biroon et.al [47] develop a monitoring system that employs a partial differential equation model to detect and isolate false data injection attacks within Cooperative Adaptive Cruise Control platoons, thereby enhancing safety and reliability. In contrast, Siddiqi et.al [48] introduce a multichain framework employing decentralized blockchain technology to enhance security against false data injection attacks in connected autonomous vehicles, thereby reducing reliance on cloud services and improving transaction throughput. Zhao et.al [49] present a cloud-based sandboxing framework designed to detect false data injection attacks in connected and automated vehicles, employing isolation techniques to enhance the safety of V2X communication systems.

Nonetheless, several limitations persist across these methodologies, including elevated false positive and negative rates, complexity in real-time applications, and reliance on computational resources. They cannot identify the injected abnormal messages with normal traffic patterns, especially for time-excitation injection attacks.

**Parameter estimation based on the Hawkes process.** Parameter estimation for the intensity function is a crucial aspect of modeling with the Hawkes process. Pan et al.[50] propose a multistage Hawkes process and used the Expectation-Maximum (EM) algorithm to solve for the Hawkes parameters. Hridoy Sankar Dutta et al.[32] use the Hawkes process to address the problem of identifying fake retweeters, applying methods such as gradient descent to

maximize the log-likelihood function for parameter estimation. For faster convergence, Yao et al.[51] employ an accelerated gradient method framework to perform parameter inference in their proposed stimuli-sensitive Hawkes process model. In practice, traditional methods such as gradient descent and the EM algorithm become challenging to compute for multidimensional Hawkes processes due to their parameter complexity, leading researchers to explore more efficient algorithms. R’emi Lemonnier[52] address this issue by developing an iterative algorithm based on adaptive matrix projection and self-concordant convex optimization, tackling the difficulties of parameter estimation in multivariate Hawkes processes. Additionally, Mei[53] apply Monte Carlo sampling to estimate gradients and optimize the event sampling process, enabling parameter estimation for multivariate Hawkes processes.

Despite these advancements, developing optimized algorithms for parameter estimation in multidimensional Hawkes processes remains a significant challenge.

## 9. Conclusion

In this paper, we propose a novel detection approach for time-exciting injection attacks inspired by real-world network security test data. We model these attacks using the MDHP and provide a closed-form solution to characterize their temporal dynamics. To facilitate parameter estimation, we develop MDHP-GDS, the first open-source gradient descent solver specifically designed for MDHP. Additionally, we integrate MDHP parameters into an LSTM-based temporal model with a residual self-attention mechanism, improving both detection accuracy and convergence speed. Experimental results show that MDHP-GDS achieves high estimation speeds and effectively distinguishes between different injection attack scenarios. Furthermore, MDHP-Net demonstrates strong detection performance, surpassing baseline methods in identifying injection attacks on IVNs.

## References

- [1] Andre Maia Pereira et al. “Automated vehicles in smart urban environment: A review”. In: *2017 Smart City Symposium Prague (SCSP)*. IEEE, 2017, pp. 1–8.
- [2] Haichun Zhang et al. “CANsec: A practical in-vehicle controller area network security evaluation tool”. In: *Sensors* 20.17 (2020), p. 4900.
- [3] Huimin Chen et al. “Towards secure intra-vehicle communications in 5G advanced and beyond: Vulnerabilities, attacks and countermeasures”. In: *Vehicular Communications* 39 (2023), p. 100548.

- [4] Xiaoqiang Sun, F Richard Yu, and Peng Zhang. “A survey on cyber-security of connected and autonomous vehicles (CAVs)”. In: *IEEE Transactions on Intelligent Transportation Systems* 23.7 (2021), pp. 6240–6259.
- [5] Marco De Vincenzi et al. “A Systematic Review on Security Attacks and Countermeasures in Automotive Ethernet”. In: *ACM Computing Surveys* 56.6 (2024), pp. 1–38.
- [6] Lei Xue et al. “{SAID}: State-aware defense against injection attacks on in-vehicle network”. In: *31st USENIX Security Symposium (USENIX Security 22)*. 2022, pp. 1921–1938.
- [7] UK Clifford. *BMW OBD Port Theft—The Solution*. website. [https://clifford.co.uk/BMW\\_OBD\\_Theft.html](https://clifford.co.uk/BMW_OBD_Theft.html). 2016.
- [8] Dawei Lyu et al. *Remote Attacks on Vehicles by Exploiting Vulnerable Telematics*. website. <https://www.yumpu.com/en/document/read/56559249/remote-attacks-on-vehicles-by-exploiting-vulnerable-telematics>. 2016.
- [9] Charlie Miller. “Remote exploitation of an unaltered passenger vehicle”. In: *Black Hat USA* (2015).
- [10] Tencent Keen Lab. *New Car Hacking Research by KeenLab: Experimental Security Assessment of BMW Cars*. website. <https://keenlab.tencent.com/zh/2018/05/22/New-CarHacking-Research-by-KeenLab-Experimental-Security-Assessment-of-BMW-Cars/>. 2018.
- [11] Tencent Keen Lab. *Keen Lab Hackers Managed to Take Control of Tesla Vehicles Again*. website. <https://electrek.co/2017/07/28/tesla-hack-keen-lab/>. 2017.
- [12] Chen BY et al. “Research Progress on Attacks and Defenses Technologies for In-vehicle Network of Intelligent Connected Vehicle”. In: *Journal of Software* (2024), pp. 1–30.
- [13] Samuel Woo, Hyo Jin Jo, and Dong Hoon Lee. “A practical wireless attack on the connected car and security protocol for in-vehicle CAN”. In: *IEEE Transactions on intelligent transportation systems* 16.2 (2014), pp. 993–1006.
- [14] Seulhui Lee, Wonsuk Choi, and Dong Hoon Lee. “Protecting some/ip communication via authentication ticket”. In: *Sensors* 23.14 (2023), p. 6293.
- [15] Kiho Lim and DJVC Manivannan. “An efficient protocol for authenticated and secure message delivery in vehicular ad hoc networks”. In: *Vehicular Communications* 4 (2016), pp. 30–37.
- [16] Zhuo Wei, Yanjiang Yang, and Tieyan Li. “Authenticated can communications using standardized cryptographic techniques”. In: *Information Security Practice and Experience: 12th International Conference, ISPEC 2016, Zhangjiajie, China, November 16-18, 2016, Proceedings 12*. Springer. 2016, pp. 330–343.
- [17] Marco Iorio et al. “Securing SOME/IP for in-vehicle service protection”. In: *IEEE Transactions on Vehicular Technology* 69.11 (2020), pp. 13450–13466.
- [18] Ivan E Carvajal-Roca et al. “A semi-centralized dynamic key management framework for in-vehicle networks”. In: *IEEE transactions on vehicular technology* 70.10 (2021), pp. 10864–10879.
- [19] Michael Müter and Naim Asaj. “Entropy-based anomaly detection for in-vehicle networks”. In: *2011 IEEE Intelligent Vehicles Symposium (IV)*. IEEE. 2011, pp. 1110–1115.
- [20] Charlie Miller and Chris Valasek. “Adventures in automotive networks and control units”. In: *Def Con* 21.260-264 (2013), pp. 15–31.
- [21] Michael Müter, André Groll, and Felix C Freiling. “A structured approach to anomaly detection for in-vehicle networks”. In: *2010 Sixth International Conference on Information Assurance and Security*. IEEE. 2010, pp. 92–98.
- [22] Kyong-Tak Cho and Kang G Shin. “Fingerprinting electronic control units for vehicle intrusion detection”. In: *25th USENIX Security Symposium (USENIX Security 16)*. 2016, pp. 911–927.
- [23] Yijie Xun, Yilin Zhao, and Jiajia Liu. “VehicleEIDS: A novel external intrusion detection system based on vehicle voltage signals”. In: *IEEE Internet of Things Journal* 9.3 (2021), pp. 2124–2133.
- [24] Wonsuk Choi et al. “VoltageIDS: Low-level communication characteristics for automotive intrusion detection system”. In: *IEEE Transactions on Information Forensics and Security* 13.8 (2018), pp. 2114–2129.
- [25] Natasha Alkhatib, Hadi Ghauch, and Jean-Luc Danger. “SOME/IP intrusion detection using deep learning-based sequential models in automotive ethernet networks”. In: *2021 IEEE 12th annual information technology, electronics and mobile communication conference (IEMCON)*. IEEE. 2021, pp. 0954–0962.
- [26] Natasha Alkhatib et al. “Here comes SAID: A SOME/IP Attention-based mechanism for Intrusion Detection”. In: *2023 Fourteenth International Conference on Ubiquitous and Future Networks (ICUFN)*. IEEE. 2023, pp. 462–467.
- [27] Alan G Hawkes. “Point spectra of some mutually exciting point processes”. In: *Journal of the Royal Statistical Society Series B: Statistical Methodology* 33.3 (1971), pp. 438–443.
- [28] Alan G Hawkes. “Spectra of some self-exciting and mutually exciting point processes”. In: *Biometrika* 58.1 (1971), pp. 83–90.
- [29] Sheldon M Ross. *Stochastic processes*. John Wiley & Sons, 1995.
- [30] Rafael Lima. “Hawkes processes modeling, inference, and control: An overview”. In: *SIAM Review* 65.2 (2023), pp. 331–374.
- [31] Izhak Rubin. “Regular point processes and their detection”. In: *IEEE Transactions on Information Theory* 18.5 (1972), pp. 547–557.
- [32] Hridoy Sankar Dutta et al. “HawkesEye: Detecting fake retweeters using Hawkes process and topic mod-

- eling”. In: *IEEE Transactions on Information Forensics and Security* 15 (2020), pp. 2667–2678.
- [33] Tohru Ozaki. “Maximum likelihood estimation of Hawkes’ self-exciting point processes”. In: *Annals of the Institute of Statistical Mathematics* 31 (1979), pp. 145–155.
- [34] P Rajesh Kanna and P Santhi. “Unified deep learning approach for efficient intrusion detection system using integrated spatial–temporal features”. In: *Knowledge-Based Systems* 226 (2021), p. 107132.
- [35] Pegah Mansourian et al. “Deep learning-based anomaly detection for connected autonomous vehicles using spatiotemporal information”. In: *IEEE Transactions on Intelligent Transportation Systems* 24.12 (2023), pp. 16006–16017.
- [36] Yanmao Man et al. “That person moves like a car: Misclassification attack detection for autonomous systems using spatiotemporal consistency”. In: *32nd USENIX Security Symposium (USENIX Security 23)*. 2023, pp. 6929–6946.
- [37] Pengzhou Cheng, Mu Han, and Gongshen Liu. “DESC-IDS: Towards an efficient real-time automotive intrusion detection system based on deep evolving stream clustering”. In: *Future Generation Computer Systems* 140 (2023), pp. 266–281.
- [38] Takashi Isobe et al. “Revisiting temporal modeling for video super-resolution”. In: *arXiv preprint arXiv:2008.05765* (2020).
- [39] S Hochreiter. “Long Short-term Memory”. In: *Neural Computation MIT-Press* (1997).
- [40] Jun Gao et al. “Omni SCADA intrusion detection using deep learning algorithms”. In: *IEEE Internet of Things Journal* 8.2 (2020), pp. 951–961.
- [41] Pytorch Contributors. *A Gentle Introduction to torch.autograd*. [https://pytorch.org/tutorials/beginner/blitz/autograd\\_tutorial.html](https://pytorch.org/tutorials/beginner/blitz/autograd_tutorial.html). 2024.
- [42] Diederik P. Kingma and Jimmy Ba. *Adam: A Method for Stochastic Optimization*. 2017. arXiv: 1412.6980 [cs.LG]. URL: <https://arxiv.org/abs/1412.6980>.
- [43] Qi Liu et al. “SISSA: Real-time Monitoring of Hardware Functional Safety and Cybersecurity with In-vehicle SOME/IP Ethernet Traffic”. In: *IEEE Internet of Things Journal* (2024).
- [44] Lotfi ben Othmane et al. “On the performance of detecting injection of fabricated messages into the can bus”. In: *IEEE Transactions on Dependable and Secure Computing* 19.1 (2020), pp. 468–481.
- [45] Haojie Ji et al. “In-Vehicle Network Injection Attacks Detection Based on Feature Selection and Classification”. In: *Automotive Innovation* 7.1 (2024), pp. 138–149.
- [46] Mubark Jedh et al. “Detection of message injection attacks onto the can bus using similarities of successive messages-sequence graphs”. In: *IEEE Transactions on Information Forensics and Security* 16 (2021), pp. 4133–4146.
- [47] Roghieh A Biroon, Zoleikha Abdollahi Biron, and Pierluigi Pisu. “False data injection attack in a platoon of CACC: Real-time detection and isolation with a PDE approach”. In: *IEEE transactions on intelligent transportation systems* 23.7 (2021), pp. 8692–8703.
- [48] Sadia Jabeen Siddiqi et al. “Multichain-Assisted Lightweight Security for Code Mutated False Data Injection Attacks in Connected Autonomous Vehicles”. In: *IEEE Transactions on Intelligent Transportation Systems* (2024).
- [49] Chunheng Zhao et al. “Detection of false data injection attack in connected and automated vehicles via cloud-based sandboxing”. In: *IEEE Transactions on Intelligent Transportation Systems* 23.7 (2021), pp. 9078–9088.
- [50] Fenglian Pan et al. “Quantifying Error Propagation in Multi-Stage Perception System of Autonomous Vehicles via Physics-Based Simulation”. In: *2022 Winter Simulation Conference (WSC)*. IEEE, 2022, pp. 2511–2522.
- [51] Mengfan Yao et al. “Stimuli-sensitive Hawkes processes for personalized student procrastination modeling”. In: *Proceedings of the Web Conference 2021*. 2021, pp. 1562–1573.
- [52] Rémi Lemonnier, Kevin Scaman, and Argyris Kalogeratos. “Multivariate Hawkes processes for large-scale inference”. In: *Proceedings of the AAAI conference on artificial intelligence*. Vol. 31. 1. 2017.
- [53] Hongyuan Mei and Jason M Eisner. “The neural hawkes process: A neurally self-modulating multivariate point process”. In: *Advances in neural information processing systems* 30 (2017).
- [54] Daryl J Daley, David Vere-Jones, et al. *An introduction to the theory of point processes: volume I: elementary theory and methods*. Springer, 2003.
- [55] Jakob Gulddahl Rasmussen. “Lecture notes: Temporal point processes and the conditional intensity function”. In: *arXiv preprint arXiv:1806.00221* (2018).
- [56] Pytorch Contributors. *Broadcasting semantics*. <https://pytorch.org/docs/stable/notes/broadcasting.html>. 2023.
- [57] “IEEE Standard for Floating-Point Arithmetic”. In: *IEEE Std 754-2019 (Revision of IEEE 754-2008)* (2019), pp. 1–84. DOI: [10.1109/IEEESTD.2019.8766229](https://doi.org/10.1109/IEEESTD.2019.8766229).
- [58] William Wen. *Introduction to torch.compile*. [https://pytorch.org/tutorials/intermediate/torch\\_compile\\_tutorial.html](https://pytorch.org/tutorials/intermediate/torch_compile_tutorial.html). 2024.

## 10. Appendix

### 10.1. Likelihood function

In Section 4, we present the structure of the likelihood function for the Multi-Dimensional Hawkes process. We will now provide the full derivation of that equation, repeated here:

$$L = \prod_{i=0}^{D-1} \prod_{t=T_i^{(0)}}^{T_i^{\text{last}}} \lambda^i(t) \cdot e^{-\int_0^{T_{\text{span}}} \lambda^i(v) dv} \quad (5)$$

Firstly, building on the foundation laid in [33], we provide a more complete derivation of the univariate Hawkes process. Equation 2 provides the intensity function for a univariate Hawkes process. Since the Hawkes process is a type of regular point process, we redefine the intensity function based on the definition of point processes [54]:

$$\lambda(t) = \frac{f(t|\mathcal{F}_{t_n})}{1 - \int_{t_n}^t f(t|\mathcal{F}_{t_n})} \quad (5a)$$

where  $f(t|\mathcal{F}_{t_n})$  is the conditional probability density function.

To calculate the likelihood function, we need to determine  $f(t|\mathcal{F}_{t_n})$ . For Equation 5a, we can further transform it as follows [55]:

$$\begin{aligned} \lambda(t) &= \frac{\frac{d}{dt}F(t|\mathcal{F}_{t_n})}{1 - F(t|\mathcal{F}_{t_n})} \\ &= -\frac{d}{dt} \ln(1 - F(t|\mathcal{F}_{t_n})) \end{aligned}$$

Integrate both sides with respect to  $t$ :

$$\int_{t_{n-1}}^t \lambda(v)dv = -\ln(1 - F(t|H_{t_n})) \quad (5b)$$

So that,

$$1 - F(t|\mathcal{F}_{t_n}) = e^{-\int_{t_n}^t \lambda(v)dv} \quad (5c)$$

We get the  $f(t|\mathcal{F}_{t_n})$  by substituting Equation 5c into Equation 5a:

$$f(t|\mathcal{F}_{t_n}) = \lambda(t) \cdot e^{-\int_{t_n}^t \lambda(v)dv} \quad (5d)$$

The likelihood function expression is given by the following equation:

$$L = f(t_1 | \mathcal{F}_0) f(t_2 | \mathcal{F}_{t_1}) \cdots f(t_n | \mathcal{F}_{t_{n-1}}) (1 - F(T | \mathcal{F}_{t_n}))$$

where  $1 - F(T | \mathcal{F}_{t_n})$  is used to denote the time of the next event  $t_{n+1}$  in the Hawkes process, which is greater than  $T$ .

So, we can get the likelihood of univariate Hawkes process:

$$\prod_{i=1}^n \lambda(t_i) \cdot e^{-\int_0^T \lambda(v)dv} \quad (5e)$$

After getting the likelihood function for the one-dimensional Hawkes process, we extend our analysis to the Multi-Dimensional Hawkes process. Here, we introduce the concept of conditional independence:

**Definition 1:** Conditional independence implies that, given the entire history, event sequences across different dimensions are mutually independent.

For random variables that satisfy conditional independence, there is an important property: their joint probability can be represented as the product of their local conditional probabilities. Clearly, the Multi-Dimensional Hawkes process satisfies conditional independence. The joint likelihood function for a Multi-Dimensional Hawkes process can be expressed as the product of the likelihoods for each dimension. Therefore, we can derive the likelihood function for the Multi-Dimensional Hawkes process as follows:

$$L = \prod_{i=0}^{D-1} \prod_{t=T_i^{(0)}}^{T_i^{\text{last}}} \lambda^i(t) \cdot e^{-\int_0^{T_{\text{span}}} \lambda^i(v)dv} \quad (5f)$$

## 10.2. Simplifications for log-likelihood function

For the proposed log-likelihood in Equation 6, we define the integral part as  $\Gamma$ :

$$\Gamma = \sum_{i=0}^{D-1} \int_0^{T_{\text{span}}} \left( \theta_i + \sum_{j=0}^{D-1} \sum_{k:T_j^k < v} \alpha^{(i,j)} e^{-\beta^{(i,j)}(v-T_j^k)} \right) dv \quad (13)$$

For  $\Gamma$ , we can further solve the integral to obtain a more simplified form. First, for the baseline intensity  $\theta$ , based on the definition of the integral, we can isolate it:

$$\sum_{i=0}^{D-1} \int_0^{T_{\text{span}}} \theta_i dv = T_{\text{span}} \sum_{i=0}^{D-1} \theta_i \quad (14)$$

Thus, we define the remaining part as  $\Gamma'$ , and further derive the following for  $\Gamma'$ :

$$\begin{aligned} \Gamma' &= \sum_{i=0}^{D-1} \sum_{j=0}^{D-1} \int_0^{T_{\text{span}}} \left( \sum_{k \text{ such that } T_j^k < t} \alpha^{(i,j)} e^{-\beta^{(i,j)}(v-T_j^k)} \right) dv \\ &= \sum_{i=0}^{D-1} \sum_{j=0}^{D-1} \alpha^{(i,j)} \int_{T_j^{\text{last}}}^{T_{\text{span}}} \left( \sum_{k=T_j^1}^{T_j^{\text{last}}} e^{-\beta^{(i,j)}(v-T_j^k)} \right) dv + \\ &\quad \sum_{i=0}^{D-1} \sum_{j=0}^{D-1} \alpha^{(i,j)} \sum_{z=1}^{\text{last}_j-1} \int_{T_j^z}^{T_j^{z+1}} \left( \sum_{k=T_j^1}^{T_j^z} e^{-\beta^{(i,j)}(v-T_j^k)} \right) dv \\ &= \sum_{i=0}^{D-1} \sum_{j=0}^{D-1} \alpha^{(i,j)} \sum_{z=1}^{\text{last}_j-1} \sum_{k=T_j^1}^{T_j^z} \left( e^{-\beta^{(i,j)}(T_j^{z+1}-T_j^k)} - e^{-\beta^{(i,j)}(T_j^z-T_j^k)} \right) \\ &\quad + \sum_{i=0}^{D-1} \sum_{j=0}^{D-1} \alpha^{(i,j)} \sum_{k=T_j^1}^{T_j^{\text{last}}} \left( e^{-\beta^{(i,j)}(T_{\text{span}}-T_j^k)} - e^{-\beta^{(i,j)}(T_j^{\text{last}}-T_j^k)} \right) \\ &= - \sum_{i=0}^{D-1} \sum_{j=0}^{D-1} \frac{\alpha^{(i,j)}}{\beta^{(i,j)}} \sum_{z=1}^{\text{last}_j} \left( e^{-\beta^{(i,j)}(T_{\text{span}}-T_j^z)} - 1 \right) \end{aligned} \quad (15)$$

Therefore, we obtain the final form of  $\Gamma$  as follows:

$$\Gamma = T_{\text{span}} \sum_{i=0}^{D-1} \theta_i - \sum_{i=0}^{D-1} \sum_{j=0}^{D-1} \frac{\alpha^{(i,j)}}{\beta^{(i,j)}} \sum_{z=1}^{\text{last}_j} \left( e^{-\beta^{(i,j)}(T_{\text{span}}-T_j^z)} - 1 \right) \quad (16)$$

## 10.3. Optimization Strategies of MDHP-GDS

In this section, we will illuminate the optimization strategies used by MDHP-GDS. First of all, Equation 7 is split into Part1, Part2, and Part3, as shown in the following equations:



$$\begin{aligned} \text{Part1} &= \sum_{i=0}^{D-1} \sum_{t=T_i^{(0)}}^{T_i^{\text{last}}} \ln \left( \theta_i + \sum_{j=0}^{D-1} \sum_{k \wedge T_j^k < t} \alpha^{(i,j)} e^{-\beta^{(i,j)} (t-T_j^k)} \right) \\ \text{Part2} &= -T_{\text{span}} \sum_{i=0}^{D-1} \theta_i \\ \text{Part3} &= \sum_{i=0}^{D-1} \sum_{j=0}^{D-1} \left( \frac{\alpha^{(i,j)}}{\beta^{(i,j)}} \sum_k \left( e^{-\beta^{(i,j)} (T_{\text{span}} - T_j^{(k)})} - 1 \right) \right) \end{aligned}$$

And  $\ln L$  can now be described as:

$$\ln L = \text{Part1} + \text{Part2} + \text{Part3}$$

For each part, as well as the initialization and execution stages, we adopted a variety of cutting-edge optimization strategies to significantly improve the computation speed of the loss function and the estimation efficiency of MDHP parameters.

**10.3.1. Initialization.** Initialization of MDHP-GDS begins by receiving a list of tensors as input data. Each tensor corresponds to a Hawkes dimension, and therefore there are `dim` tensors in total.

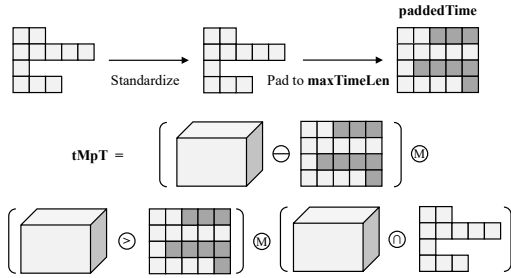


Figure 15: Initialization process.

*Standardization* — As illustrated in Figure 15, a standardization process governed by Equation 17 is applied to every tensor in the input list. This transformation preserves the original distribution shape while scaling the data to a specified range between *Max* and *Min*, aligns the data across various inputs, ensuring consistency and promoting faster convergence during the training phase.

$$T = \frac{T - \min(T)}{\max(T) - \min(T)} * (\text{Max} - \text{Min}) + \text{Min} \quad (17)$$

*Padding* — Although timestamps within each tensor are sorted in ascending order, the tensors often vary in length. This discrepancy in size leads to inefficient data storage and decreased computational performance. To address this problem, we pad each tensor to the length of the longest tensor, `maxTimeLen`, and then stack the tensors into a continuous 2-D array with the shape `(dim, maxTimeLen)`.

*Decoupling* — A key part of the initialization involves decoupling computations that are unrelated to the gradient

descent process. A significant portion of these unrelated calculations is embedded in Part1:

$$\text{Part1} = \sum_{i=0}^{D-1} \sum_{t=T_i^{(0)}}^{T_i^{\text{last}}} \dots \sum_{j=0}^{D-1} \sum_{k \wedge T_j^k < t} \dots (t - T_j^k)$$

This nested calculation poses challenges for two main reasons: (1)  $T_i^{\text{last}}$  differs for each dimension, and (2) the constraint  $k \wedge T_j^k < t$  complicates the loop structure. Fortunately, the first issue has been resolved by padding the tensors into  $T_{\text{padded}}$ , ensuring uniform tensor lengths. We alleviate the second issue by constructing a 4-D tensor `tMpT` (i.e.,  $t - T_{\text{padded}}$ ) with shape `(dim, maxTimeLen, dim, maxTimeLen)`. When it is necessary, we can easily mask out irrelevant portions from  $t - T_j^k$  to streamline the loop and eliminate unwanted calculations.

**10.3.2. Part1.** The computational complexity of Part1 is heightened by its structure, which includes four nested loops and intricate boundary conditions. Traditionally, this form of loop-heavy computation becomes notably sluggish, particularly when executed explicitly in interpreted languages such as Python. However, at the initialization stage, the utilization of  $T_{\text{padded}}$  allows for the pre-computation of the 4-D tensor `tMpT`, which facilitates the computation with underlying vectorized operations and later broadcasting technique.

---

**Algorithm 1** Calculation of  $\ln L$  : Part1

---

**Input:** `tMpT`,  $\alpha$ ,  $\beta$ ,  $\theta$

**Output:** Result

```

 $\alpha \leftarrow \text{expand}(\alpha,[:,1, :, 1])$ 
 $\beta \leftarrow \text{expand}(\beta,[:,1, :, 1])$ 
 $\theta \leftarrow \text{expand}(\theta,[:,1, :, 1])$ 
 $A_{\text{exp}} \leftarrow \alpha * \exp(\text{clamp\_max}(-\beta * \text{tMpT}, 80))$ 
 $S \leftarrow \text{sum}(A_{\text{exp}}, \text{dim} = [2, 3])$ 
Result  $\leftarrow \text{sum}(\log(\theta + S))$ 

```

---

*Broadcasting* — We employ the vector broadcasting technique to perform vectorized calculations across higher dimensions initially with the help of automatic-broadcasting mechanism in Pytorch [56], then refining our focus to lower dimensions. This approach is detailed in Algorithm 1, which demonstrates how to pre-expand the parameters  $\alpha$ ,  $\beta$ , and  $\theta$ . Subsequently, these parameters are applied across specific dimensions to yield the final scalar output of Part1, achieving a more efficient and streamlined processing workflow.

*Clamping* — Clamping is a critical step in the computation of exponential functions, particularly when handling data of type FP32 under IEEE754 standard [57]. In this context, we impose a constraint that all elements must remain below a threshold of 80. This precaution is necessary because values exceeding this limit can cause the exponential results to overflow, leading to inaccuracies in calculations.

**10.3.3. Part2.** Part2 is the easiest part to calculate, as shown in Algorithm 2.

---

**Algorithm 2** Calculation of  $\ln L$  : Part2

---

**Input:**  $T_{\text{span}}, \theta$ **Output:** Result

$$\text{Result} \leftarrow -T_{\text{span}} * \text{sum}(\theta)$$

---

**10.3.4. Part3.** Similar to Part1, the optimization of Part3 also leverages automatic broadcasting techniques and clamping operations to enhance computational efficiency. The key distinction for Part3, however, lies in its simpler loop structure. Consequently, the input parameters  $\beta$  and  $T_{\text{padded}}$  are extended to a 3-D tensor. This reduction in dimensionality not only decreases the memory usage but also lessens the computational load.

---

**Algorithm 3** Calculation of  $\ln L$  : Part3

---

**Input:**  $T_{\text{padded}}, T_{\text{span}}, \alpha, \beta$ **Output:** Result

$$\begin{aligned} T_{\text{bcasted}} &\leftarrow \text{expand}(T_{\text{padded}},[:, \text{dim}, :]) \\ \beta &\leftarrow \text{expand}(\beta,[:, :, 1]) \\ K_{\text{inner}} &\leftarrow \text{clamp\_max}(-\beta * (T_{\text{span}} - T_{\text{bcasted}}), 80) \\ K_{\text{inner}} &\leftarrow \text{transpose}(\text{exp}(K_{\text{inner}}), (0, 1)) \\ K_{\text{sum}} &\leftarrow \text{sum}(K_{\text{inner}}, \text{dim} = 2) \\ \text{Result} &\leftarrow \text{sum}(\alpha/\beta * K_{\text{sum}}) \end{aligned}$$

---

The specific methods and procedures utilized in this optimization process are detailed in Algorithm 3. This pseudocode outlines how the reduced complexity and streamlined data structure contribute to faster processing times while maintaining accuracy, thereby optimizing the performance of the underlying calculations in the gradient descent process.

**10.3.5. JIT Compilation.** Just-In-Time (JIT) compilation is a dynamic method of code compilation that offers a balance between the performance benefits of ahead-of-time (AOT) compilation and the flexibility of interpretation. The principle behind JIT compilation lies in its ability to compile portions of the code during runtime, thereby optimizing the execution speed without requiring a full pre-compilation of the script.

In the latest PyTorch (at least 2.0), `torch.compile` is a simple yet efficient method to speed up PyTorch code, which compiles a function to a fused and optimized kernel with minimal code changes [58]. In practice, we decorate the loss function consisting of three parts with `torch.compile` decorator, and the JIT compilation will be automatically applied in both in CPU and GPU mode.

## 10.4. Detailed Dataset Description

Table 10 exhibits part of the simulation data. Each SOME/IP message consists of data fields such as Timestamp, Source Address, Destination Address, etc. The data is generated by multiple open-source projects introduced in Section 6.1.2 to ensure the reliability.

Table 10: Simulation data.

Time	src	dst	met	len	cl	se	pro	in	Message_Type	Err_Code
$t_1$	10.1.0.8	10.0.0.2	2	25	8	80	1	1	NOTIFICATION	E_OK
$t_2$	10.1.0.2	10.0.0.6	1	26	6	85	1	1	RESPONSE	E_OK
$t_3$	10.1.0.2	10.0.0.2	1	25	2	97	1	1	RESPONSE	E_OK
$t_4$	10.1.0.6	10.0.0.2	1	11	6	94	1	1	REQUEST	E_OK
$t_5$	10.0.0.2	10.1.0.3	1	20	3	70	1	1	RESPONSE	E_OK
$t_6$	10.1.0.2	10.0.0.3	1	27	3	70	1	1	RESPONSE	E_OK
$t_7$	10.1.0.2	10.0.0.3	1	10	3	91	1	1	ERROR	EMALFORMED_MESSAGE
$t_8$	10.0.0.2	10.1.0.3	1	13	3	71	1	1	ERROR	E_NOT_OK
$t_9$	10.1.0.2	10.0.0.8	1	11	8	67	1	1	RESPONSE	E_OK
$t_{10}$	10.1.0.1	10.0.0.5	273	24	5	79	1	1	ERROR	E_NOT_OK
$t_{11}$	10.0.0.6	10.1.0.3	1	10	6	12	1	1	REQUEST	E_OK

src: Source addresses; dst: Destination addresses; met: Method; len: Length; cl: Client; se: Session; pro: Protocol; in: Interface.

## 10.5. CDF Curves of Different Dims

Figure 16 shows the CDF curves in more MDHP dimensions. It is obvious that, in most cases, MDHP parameters can be a significant feature in classifying normal and attack message windows.

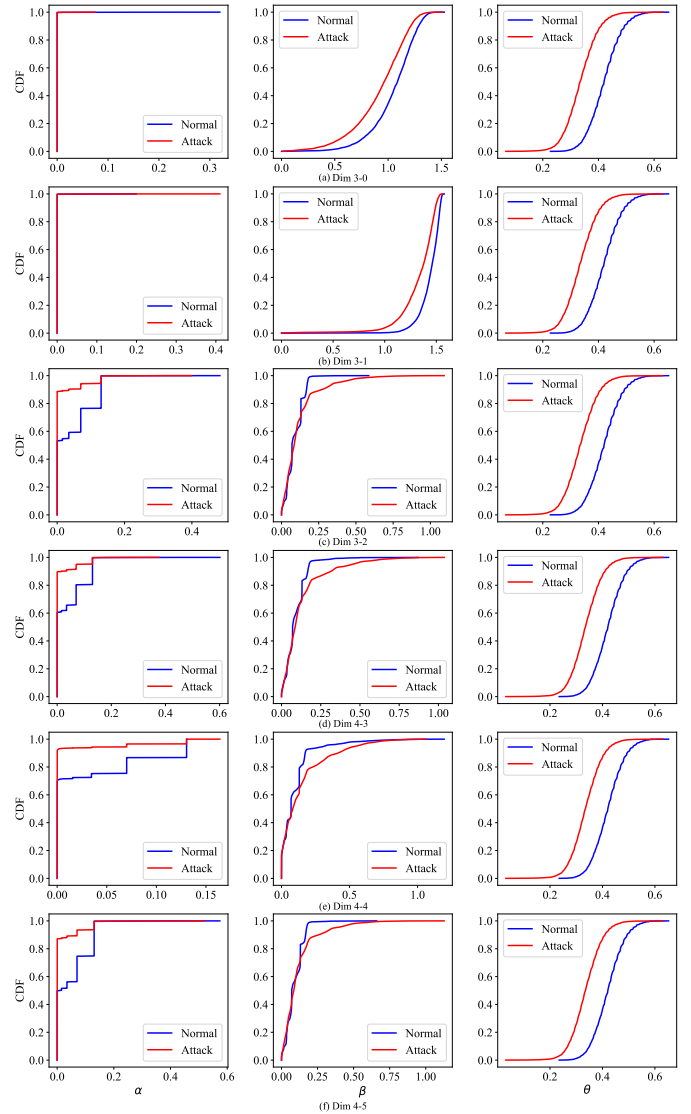


Figure 16: CDF of Different MDHP dimensions